Toward Intrinsic Ferroelectric Switching in Multiferroic $BiFeO_3$

Eric Parsonnet,[1,*] Yen-Lin Huang,[2] Tanay Gosavi,[3] Alexander Qualls,[1] Dmitri Nikonov,[3] Chia-Ching Lin,[3] Ian Young,[3] Jeffrey Bokor,[4] Lane W. Martin,[2,5] and Ramamoorthy Ramesh[1,2,5,†]

[1]*Department of Physics, University of California, Berkeley, California 94720, USA*
[2]*Department of Materials Science and Engineering, University of California, Berkeley, California 94720, USA*
[3]*Components Research, Intel Corporation, Hillsboro, Oregon 97124, USA*
[4]*Department of Electrical Engineering and Computer Science, University of California, Berkeley, California 94720, USA*
[5]*Materials Sciences Division, Lawrence Berkeley National Laboratory, Berkeley, California 94720, USA*

(Received 25 January 2020; revised 23 June 2020; accepted 20 July 2020; published 6 August 2020)

Using pulsed ferroelectric measurements, we probe switching dynamics in multiferroic $BiFeO_3$, revealing low-ns switching times and a clear pathway to sub-ns switching. Our data is well described by a nucleation and growth model, which accounts for the various timescales in the switching process, namely (1) the ferroelectric polarization switching (bound-charge) dynamics and (2) the *RC*-limited movement of free charge in the circuit. Our model shows good agreement with observed data and begins to bridge the gap between experiment and theory, indicating pathways to study ferroelectric switching on intrinsic timescales.

DOI: 10.1103/PhysRevLett.125.067601

As a room-temperature multiferroic material, $BiFeO_3$ (BFO) has attracted much attention as a leading candidate for magnetoelectric applications. One promising example is a novel magnetoelectric spin orbit logic device with intrinsic nonvolatility [1]. While there has been extensive work on quasistatic magnetoelectric coupling in BFO, and electric-field control of magnetization has been experimentally demonstrated [2,3], the dynamics, fundamental speed limits, and mechanisms of ferroelectric and magnetoelectric switching on intrinsic timescales are largely unexplored. One theoretical study using a first-principles-based effective Hamiltonian within molecular-dynamics simulations predicted ultrafast (∼ps) switching of both ferroelectric and magnetic order in BFO [4] and various theoretical works have predicted ferroelectric switching times on the order of tens of ps [5,6]. In proper ferroelectrics, it has often been speculated that the limit on switching speed is imposed by an acoustic-phonon mode (approximately the velocity of sound), which sets a limit on domain-wall propagation speed. For example, one would expect that switching 100 nm of a prototypical ferroelectric such as $PbZr_{1-x}Ti_xO_3$ (velocity of sound ≈2500 m/s [7]), would take ≈40 ps. There have been numerous experimental studies of switching kinetics in ferroelectrics, both in bulk and thin films [8–15]; however, these experiments detail a wide range of switching times, and generally report times considerably longer than those predicted by theory. To date, experimental observations of ultrafast switching have been limited, with only a few works approaching the low-ns timescale [16–18] and only one reporting a switching time of hundreds of ps [7]. Importantly, and almost ubiquitously in the literature, switching studies claim convolution between the switching time of the ferroelectric and *RC* effects from the measurement circuit. Using an electrical test setup that is capable of accessing timescales on the order of hundreds of ps, we measure the switching dynamics of thin-film $Bi_{0.85}La_{0.15}FeO_3$ (LBFO) and BFO. Our data show a pathway to sub-ns switching, which is a key milestone for device applications [1]. We develop a model for switching which accounts for free-charge dynamics in the measurement circuit (i.e., *RC* effects and parasitics) and demonstrate that such a model accurately describes switching in (L)BFO capacitors as well as a variety of other thin-film ferroelectrics. Finally, the model sheds light on the large disparities in experimentally observed switching times, and provides motivation to study switching on intrinsic timescales.

We perform pulsed measurements of ferroelectric polarization switching (Fig. 1, Supplemental Material [19], Sec. 1, Fig. S1). A sequence of three pulses [Fig. 1(a)], each with nominal rise time of 70 ps (applied using a Berkeley Nucleonics BN765 fast rise time pulse generator), is used to first preset the ferroelectric capacitor, second measure the switching current transient [Fig. 1(c)], and third measure the nonswitching current transient [Fig. 1(d)] of the circuit. Current transients are detected via a TEKTRONIX TDS 6604 Digital Storage Oscilloscope (6 GHz, 20 GS/s). By subtracting the nonswitching transient from the switching transient, we determine the contribution to measured current arising from switching of the ferroelectric polarization alone [7,16–18]. Any contribution to currents arising from leakage, interfacial Schottky barriers and nonlinear dielectric effects (present in all ferroelectric capacitors [20–24]) is subtracted out when

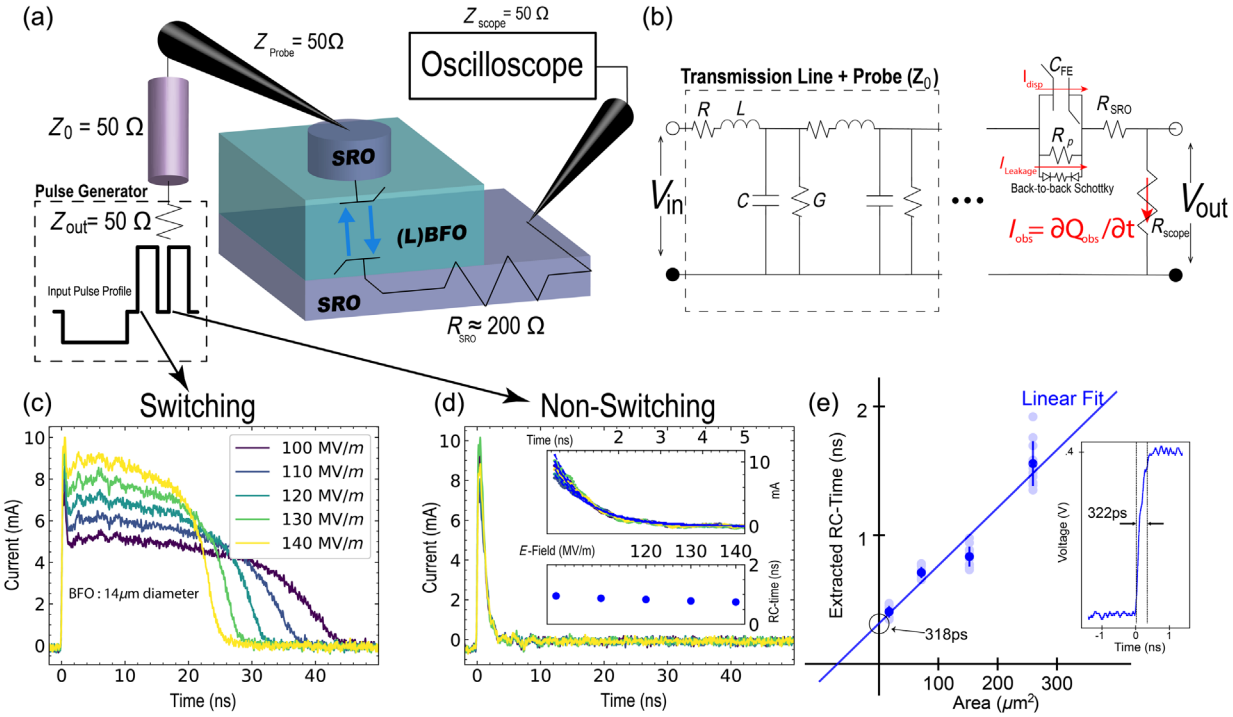

FIG. 1. Panel (a) shows a schematic of the measurement setup and input pulse profile, with effective circuit shown in (b). We show switching and nonswitching current responses for BFO capacitors in (c) and (d), respectively. The *RC*-curve fits shown in the inset of (d) indicate the *RC* time of the measurement circuit is independent of voltage. In (e) we observe linear scaling of measurement circuit *RC* time with ferroelectric device area. The inset in (e) shows the rising edge of an input pulse through the identical circuit with ferroelectric capacitor removed.

we analyze the difference between the switching and nonswitching current transients.

Pulsed measurements of ferroelectric capacitors are, by necessity, performed within the context of a measurement circuit which imposes additional constraints. As highlighted [Figs. 1(a) and 1(b)], careful consideration of the complete circuit is required to understand ferroelectric switching in such configurations. The transmission line delivering and collecting the signal is impedance matched from the pulse generator to the probe tip (DCP-150R coaxial probes: characteristic impedance of 50 Ω) and from the probe tip to the oscilloscope. To quantitatively measure the parasitics in the circuit, we extract, via fitting of the nonswitching pulse current response to an *RC* curve, the *RC* time of the measurement circuit and find that it is independent of applied voltage [Fig. 1(d), insets] and scales linearly with the area of the ferroelectric capacitor being studied [Fig. 1(e)]. The latter observation indicates that the measurement circuit capacitance is dominated by the ferroelectric device under study. Via extrapolation of the extracted *RC* time dependence on device area, we are able to determine the effective timescale of the parasitics of the circuit to be ∼318 ps [Fig. 1(e)], which matches well with the observed rise time of a pulse through the identical circuit with the ferroelectric capacitor removed [Fig. 1(e)].

To better understand the mechanisms and limits on ferroelectric switching we use high quality (Supplemental Material [19], Sec. 2, Fig. S2) epitaxial ferroelectric thin films with systematically tuned spontaneous polarization and study switching under a range of applied electric fields and device sizes. All samples have symmetric top and bottom $SrRuO_3$ (SRO) electrodes. By integrating the difference between the switching and nonswitching response current, we obtain the polarization transient [Fig. 2(a), Supplemental Material [19], Sec. 3, Fig. S3) and extract the switching time, defined as the time when the switched polarization reaches 90% of its saturation value [vertical lines in Fig. 2(a)]. We show extracted switching time as a function of applied field for 20-nm-thick BFO and LBFO films [Fig. 2(b)]. As observed, the LBFO consistently switches faster than its BFO counterpart.

Within the BFO system, it has been shown experimentally that lanthanum substitution reduces the rhombohedral distortion thereby lowering the magnitude of the remnant polarization and the coercive field [25,26]. Similarly, density-functional-theory calculations show that lanthanum substitution reduces both the potential-energy barrier between, and magnitude of, the degenerate ground states of polarization [25,26]. This systematic change in the free-energy landscape manifests itself as a lowering of the activation energy for switching. Similar dependence on the

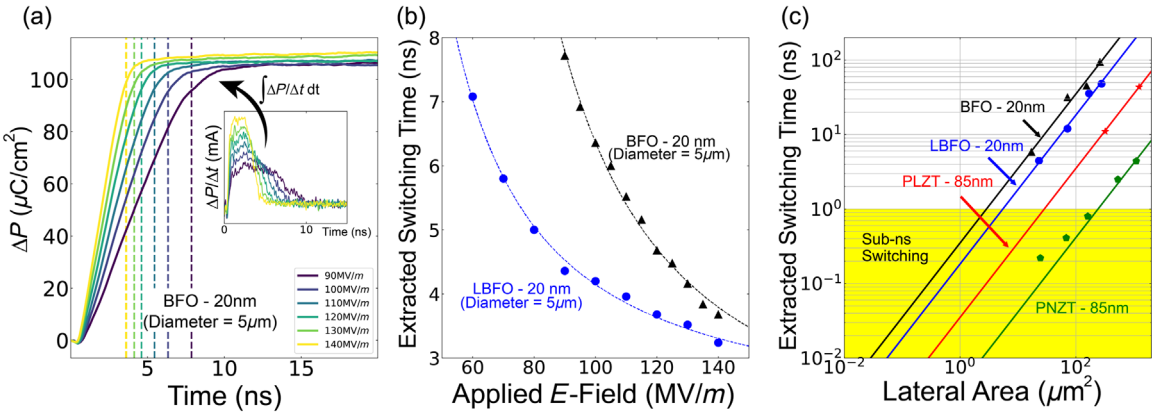

FIG. 2. Panel (a) shows the polarization transient, determined by integrating the difference between the switching and nonswitching current response in the system (inset). Dashed vertical lines show extracted switching time, defined as the time when polarization reached 90% of saturation. (b) shows experimentally observed switching times for 20 nm-thick $BiFeO_3$ (BFO) and 20-nm-thick $Bi_{0.85}La_{0.15}FeO_3$ (LBFO) as a function of applied field. The data reveals low-ns switching (dashed lines provide a guide to the eye). Panel (c) shows switching time as a function of area for the following samples: 20 nm $BiFeO_3$ (BFO), 20 nm $Bi_{0.85}La_{0.15}FeO_3$ (LBFO), 85 nm $Pb_{.9}La_{.1}[Zr_{.2}Ti_{.8}]O_3$ (PLZT) and 85 nm Pb $[Nb_{.04}Zr_{.29}Ti_{.67}]O_3$ (PNZT). Solid lines are linear best fits. The data shown are at an applied field of 95, 95, 26, and 60 MV/m for BFO, LBFO, PLZT, and PNZT, respectively. We include similar data for all samples and applied fields in this study (Supplemental Material [19], Fig. S4).

spontaneous polarization (or, conversely, the spontaneous structural distortion) is also observed in other ferroelectrics [Fig. 3(a)]. For example, a $Pb_{0.9}La_{0.1}[Zr_{0.2}Ti_{0.8}]O_3$ (PLZT) sample, with a switchable polarization of $\sim 15\ \mu C/cm^2$ switches much faster than the (L)BFO, with a switchable polarization $\sim(80)100\ \mu C/cm^2$. We show switching times as a function of lateral device area for LBFO, BFO, PLZT, and $Pb[Nb_{0.04}Zr_{0.29}Ti_{0.67}]O_3$ (PNZT) (extracted from [27]) [Fig. 2(c)] for single applied fields and include extended results for LBFO, BFO, and PLZT for several applied fields (Supplemental Material [19], Sec. 4, Fig. S4). In all cases, a similar trend is observed, wherein there is a linear scaling with capacitor area. As such, the data presented provide a pathway to sub-ns switching for capacitor areas of $\leq 5\ \mu m^2$ for LBFO.

We develop a scheme to compare switching times across materials and device sizes. By rescaling the extracted switching time (90% of switched polarization saturation) as: $t_s \rightarrow t_s \times t_{FE}/(AR)$ where t_{FE}, A, and R are the thickness of the ferroelectric, device area, and external resistance, respectively [Fig. 1(a)], we can map switching-time data onto families of curves (plotted as switching time vs applied electric field), which depend only on the ferroelectric material (Fig. 3). Since the capacitance of the circuit is dominated by ferroelectric capacitor [Fig. 1(e)] the ratio RA/t_{FE} enters directly into the calculation for the RC time of the circuit. We note that in performing the rescaling (Fig. 3), we account for the extrinsic factors impacting the RC time of the measurement circuit, revealing dynamics dependent on material alone. The success of such rescaling illustrates an effective way to compare switching speeds across samples and materials.

When studying ferroelectric switching, we must account for the charge dynamics of the entire system, including the measurement circuit and parasitics inside and outside the ferroelectric capacitor (e.g., leakage current, nonlinear

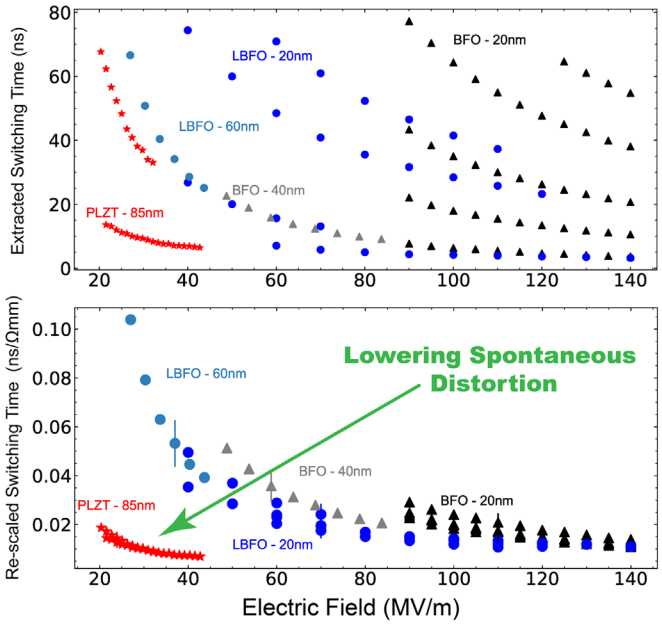

FIG. 3. The top panel shows switching time data for a variety of measurements as a function of applied field. We vary composition, thickness and lateral capacitor size and find a broad spread in data. Decreasing capacitor size correlates with faster switching time. In the bottom panel we rescale switching time as $t_s \rightarrow t_s \times t_{FE}/(AR)$ and collapse all data points of a single composition onto a single curve, providing a protocol for comparing switching times across materials and samples.

dielectric response, external resistance and capacitance, and electrode-ferroelectric interfacial Schottky barriers). The total observed current ($I_{\rm obs}$) is comprised of the sum of displacement and leakage (I_L) currents. Displacement current has three contributions; ferroelectric switching ($I_{\rm FE}$), linear dielectric response ($I_{\rm LD}$), and nonlinear dielectric response ($I_{\rm NLD}$).

$$I_{\rm obs} = I_L + I_{\rm FE} + I_{\rm LD} + I_{\rm NLD} \tag{1}$$

The observed current ($I_{\rm obs}$), the displacement current ($I_{\rm disp} = I_{\rm FE} + I_{\rm LD} + I_{\rm NLD}$), and the (leakage) current (I_L) arising from Schottky barriers [20–24,28,29] at the metal and ferroelectric interfaces and resistive leakage in the ferroelectric [Fig. 1(b)] are given by:

$$I_{\rm obs} = \frac{V_{\rm in} - V_{\rm FE}}{R}, \tag{2}$$

$$I_{\rm disp} = \frac{V_{\rm in} - V_{\rm FE}}{R} - I_L, \tag{3}$$

$$I_L = A\frac{2J_{S1}J_{S2}\sinh\frac{qV_{\rm FE}}{2kT}}{J_{S1}\exp[-\frac{qV_{\rm FE}}{2kT}] + J_{S2}\exp[\frac{qV_{\rm FE}}{2kT}]} + V_{\rm FE}/R_P, \tag{4}$$

where R, $V_{\rm in}$, $V_{\rm FE}$, I_L, A, q, T, and k are the external resistance, applied voltage, voltage across the ferroelectric, current through the back-to-back Schottky diodes with a series resistance [Fig. 1(b)] [30,31] and parallel resistor ($R_{\rm P}$), device area, elementary charge, temperature, and Boltzmann constant, respectively. $J_{S1,S2} \equiv A^*T^2\exp\left[-(q\Phi_{b1,b2}/kT)\right]$, where A^* is the Richardson constant, and $\Phi_{b1,b2}$ is the Schottky barrier at the interfaces [30,31]. The simulated (Fig. 4) maximum leakage current is $\sim$10 μA, similar to the observed steady state leakage current [Fig. 1(d)] of $\sim$4 μA. For a complete list of parameters used herein, see the Supplemental Material [19], Sec. 5. The charge on the ferroelectric capacitor ($Q_{\rm cap}$) is given by:

$$Q_{\rm cap} = A(\epsilon_0\epsilon_r E_{\rm FE} + P), \tag{5}$$

where $E_{\rm FE}$, ϵ_0, ϵ_r, and P, are the electric field across the ferroelectric, vacuum dielectric constant, relative permittivity, and average ferroelectric polarization, respectively.

Combining Eqs. (2)–(5), we find:

$$\frac{dQ_{\rm obs}}{dt} = \frac{1}{R}\left[V_{\rm in} - \frac{t_{\rm FE}(Q_{\rm cap}/A - P)}{\epsilon_0\epsilon_r}\right] \tag{6}$$

$$\frac{dQ_{\rm cap}}{dt} = \frac{1}{R}\left[V_{\rm in} - \frac{t_{\rm FE}(Q_{\rm cap}/A - P)}{\epsilon_0\epsilon_r}\right] - I_L \tag{7}$$

In the limit $I_L \to 0$, Eqs. (6) and (7) reduce to Eq. (4) of [32].

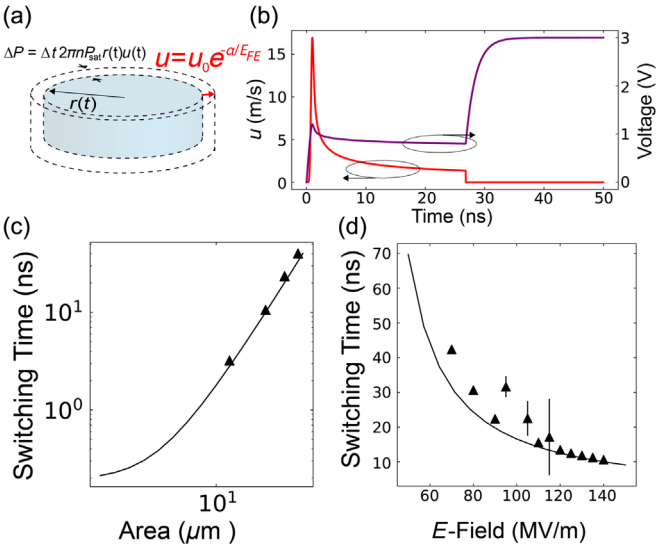

FIG. 4. Panel (a) shows a schematic of a single growing (radially) cylindrical domain with instantaneous radius $r(t)$ and domain-wall velocity $u(t)$ given by Merz's law. The change in polarization for many domains, with density n, ΔP, is given for an infinitesimal time step Δt. In (b) we show simulated voltage and domain-wall velocity transient profiles during ferroelectric switching. Panel (c) shows measured switching time for 140 MV/m applied field in 20-nm-thick BFO (points) and simulated switching time (solid line) as a function of area. The asymptote is that of the "domain growth limit." Panel (d) shows switching time for 14 μm diameter 20-nm-thick BFO capacitors (points) and simulated switching time (solid line) as a function applied field. For a full list of parameters used in the simulation see Supplemental Material [19], Sec. 5.

Polarization reversal in ferroelectrics has been successfully described by a nucleation and growth model [5,33–35] where domain-wall motion determines switching speed. Thus, domain-wall velocity is of the utmost importance in this process. In his seminal work on polarization reversal, Merz found the domain-wall velocity (u) to be empirically described by [8,9]:

$$u = u_0 e^{-\alpha/E_{\rm FE}}, \tag{8}$$

where u_0, α, $E_{\rm FE}$, are the domain-wall velocity at infinite applied field, the activation field (related to the double-well structure of the Landau free-energy landscape), and the electric-field across the ferroelectric, respectively. Merz's law has been used since its conception, and it is commonly found that the activation field is $\approx 10E_c$ where E_c is the coercive field [36].

Merz's law provides a framework to describe the average polarization dynamics of the film. We assume nucleation and growth of cylindrical domains [Fig. 4(a)], yielding the rate of change of polarization:

$$\frac{dP}{dt}(t) = 2\pi n r(t)u(t)P_{\rm sw} = 2\pi n u(t)P_{\rm sw}\int_0^t u(t')dt', \tag{9}$$

where n, $r(t) = \int_0^t u(t')dt'$, $u(t)$, P_{sw} are the areal density of nucleated domains, instantaneous domain radius, instantaneous domain-wall velocity, and switchable polarization, respectively. Equations (6)–(9) define a system of equations which are simultaneously solved numerically, yielding polarization, observed current, domain-wall velocity, and voltage across the ferroelectric as a function of time. We approximate the relative permittivity as constant [25] for the present simulations. Increased leakage current will slow polarization reversal as the voltage across the ferroelectric will be reduced. Here, the observed leakage current is ≥ 4 orders of magnitude smaller than displacement current (Fig. 1), and thus contributes only a small (∼mV) change in voltage. We compare (Supplemental Material [19], Sec. 6, Fig. S5) resistive versus Schottky emission leakage current and show that even for reduced parallel resistances the effect on switching polarization is minimal in macroscopic device structures.

The model reveals a transient voltage profile across the ferroelectric [Fig. 4(b)] akin to a negative-capacitance transient [32,37–39]. The physical origin of the time-dependent voltage and domain-wall velocity profile [Fig. 4(b)] can be explained as a competition between free- and bound-charge dynamics and is described in detail in Supplemental Material [19], Sec. 7. We explore the role of the magnitude of switchable polarization (Supplemental Material [19], Sec. 8, Fig. S6) and characterize the peak in voltage (and in domain-wall velocity) observed during ferroelectric switching (Supplemental Material [19], Sec. 9, Fig. S7). Based on our model, we can extract the area and field dependence of the switching time [Figs. 4(c) and 4(d)]. For fixed capacitor dimensions, this model is in close agreement with the experimental data of the field dependence of the switching time [Fig. 4(d)]. The areal scaling is consistent with the experimental data [Figs. 4(c) and 2(c)]; however, for smaller device sizes, we begin to observe asymptotic behavior [similar to the PNZT data, Fig. 2(c), see extended discussion in Supplemental Material [19], Sec. 10]. A likely origin of the asymptote in areal scaling is the rise time of the measurement circuit (which includes parasitics) and the device under study. This sets an "extrinsic" limit to switching speed whereby the switching cannot occur faster than the stimulus. When the parasitics of the circuit do not limit switching, the asymptotic behavior can arise due to an intrinsic "domain-growth limit," defined as the time it takes for adjacent growing domains to coalesce at maximum velocity (i.e., $\sim u_0/\sqrt{n}$). A final possibility is "intrinsic" switching whereby nucleation and growth is no longer the switching mechanism. This would occur at very small thicknesses or lateral device sizes, likely on the order of the critical nucleus size [5] or in systems in which nucleation and growth can be sufficiently suppressed.

In summary, we present direct measurements of the polarization switching dynamics in the (L)BFO model system. Our experimental measurements show a clear pathway to sub-ns switching times for capacitor areas less than $\sim 5\ \mu m^2$. Our model accurately predicts the scaling observed experimentally and presents an possible avenue to explain the wide disparity in switching times reported in the literature. Intrinsic ferroelectric switching, and mechanisms pertaining to that process, is convoluted in current switching experiments by the competition between free- and bound-charge dynamical timescales. Careful consideration of the free- and bound-charge dynamics within the framework of the measurement circuit might explain why different measurements have yielded dramatically different results. While device scaling offers a viable pathway to sub-ns switching, it remains an important question to address the limits of such scaling, which will provide vital insight into intrinsic ferroelectric switching speeds and mechanisms.

E. P. would like to thank Abel Fernandez and Lucas Caretta for bountiful discussions and acknowledges support from the Intel/FEINMAN program. J. B. and R. R. acknowledge support from the SRC-ASCENT Center, which is part of the SRC JUMP program. Y.-L. H. and L. W. M. acknowledge support from the LBNL LDRD program on Beyond Moore's Law Electronics.

*Corresponding author.
e.parsonnet@berkeley.edu
†Corresponding author.
rramesh@berkeley.edu

[1] S. Manipatruni, D. E. Nikonov, and I. A. Young, Nat. Phys. **14**, 338 (2018).
[2] J. T. Heron, J. L. Bosse, Q. He, Y. Gao, M. Trassin, L. Ye, J. D. Clarkson, C. Wang, J. Liu, S. Salahuddin, D. C. Ralph, D. G. Schlom, J. Íñiguez, B. D. Huey, and R. Ramesh, Nature (London) **516**, 370 (2014).
[3] M. Trassin, J. D. Clarkson, S. R. Bowden, J. Liu, J. T. Heron, R. J. Paull, E. Arenholz, D. T. Pierce, and J. Unguris, Phys. Rev. B **87**, 134426 (2013).
[4] S. Bhattacharjee, D. Rahmedov, D. Wang, J. Íñiguez, and L. Bellaiche, Phys. Rev. Lett. **112**, 147601 (2014).
[5] Y.-H. Shin, I. Grinberg, I.-W. Chen, and A. M. Rappe, Nature (London) **449**, 881 (2007).
[6] V. Boddu, F. Endres, and P. Steinmann, Sci. Rep. **7**, 806 (2017).
[7] J. Li, B. Nagaraj, H. Liang, W. Cao, C. H. Lee, and R. Ramesh, Appl. Phys. Lett. **84**, 1174 (2004).
[8] W. J. Merz, J. Appl. Phys. **27**, 938 (1956).
[9] W. J. Merz, Phys. Rev. **95**, 690 (1954).
[10] G. Vizdrik, S. Ducharme, V. M. Fridkin, and S. G. Yudin, Phys. Rev. B **68**, 094113 (2003).
[11] J. Y. Jo, H. S. Han, J.-G. Yoon, T. K. Song, S.-H. Kim, and T. W. Noh, Phys. Rev. Lett. **99**, 267602 (2007).
[12] R. Gaynutdinov, M. Minnekaev, S. Mitko, A. Tolstikhina, A. Zenkevich, S. Ducharme, and V. Fridkin, Physica (Amsterdam) **424B**, 8 (2013).

[13] J. Y. Jo, D. J. Kim, Y. S. Kim, S.-B. Choe, T. K. Song, J.-G. Yoon, and T. W. Noh, Phys. Rev. Lett. **97**, 247602 (2006).
[14] H. Chang, S. V. Kalinin, S. Yang, P. Yu, S. Bhattacharya, P. P. Wu, N. Balke, S. Jesse, L. Q. Chen, R. Ramesh, S. J. Pennycook, and A. Y. Borisevich, J. Appl. Phys. **110**, 052014 (2011).
[15] C. Alessandri, P. Pandey, A. Abusleme, and A. Seabaugh, IEEE Electron Device Lett. **39**, 1780 (2018).
[16] A. Grigoriev, M. M. Azad, and J. McCampbell, Rev. Sci. Instrum. **82**, 124704 (2011).
[17] P. K. Larsen, G. L. M. Kampscher, M. J. E. Ulenaers, G. A. C. M. Spierings, and R. Cuppens, Appl. Phys. Lett. **59**, 611 (1991).
[18] M. Si, X. Lyu, P. R. Shrestha, X. Sun, H. Wang, K. P. Cheung, and P. D. Ye, Appl. Phys. Lett. **115**, 072107 (2019).
[19] See the Supplemental Material at http://link.aps.org/supplemental/10.1103/PhysRevLett.125.067601 for extended data, model derivation, and discussion.
[20] E. Miranda, D. Jimnez, A. Tsurumaki-Fukuchi, J. Blasco, H. Yamada, J. Su, and A. Sawa, Appl. Phys. Lett. **105**, 082904 (2014).
[21] G. W. Pabst, L. W. Martin, Y.-H. Chu, and R. Ramesh, Appl. Phys. Lett. **90**, 072902 (2007).
[22] S. Y. Yang, L. W. Martin, S. J. Byrnes, T. E. Conry, S. R. Basu, D. Paran, L. Reichertz, J. Ihlefeld, C. Adamo, A. Melville, Y.-H. Chu, C.-H. Yang, J. L. Musfeldt, D. G. Schlom, J. W. Ager, and R. Ramesh, Appl. Phys. Lett. **95**, 062909 (2009).
[23] S. Hong, T. Choi, J. H. Jeon, Y. Kim, H. Lee, H.-Y. Joo, I. Hwang, J.-S. Kim, S.-O. Kang, S. V. Kalinin, and B. H. Park, Adv. Mater. **25**, 2339 (2013).
[24] D. Chen, A. Li, and D. Wu, J. Mater. Sci. Mater. Electron. **25**, 3251 (2014).
[25] L. Zhang, Y.-L. Huang, G. Velarde, A. Ghosh, S. Pandya, D. Garcia, R. Ramesh, and L. W. Martin, APL Mater. **7**, 111111 (2019).
[26] B. Prasad, Y.-L. Huang, R. V. Chopdekar, Z. Chen, J. Steffes, S. Das, Q. Li, M. Yang, C.-C. Lin, T. Gosavi, D. E. Nikonov, Z. Q. Qiu, L. W. Martin, B. D. Huey, I. Young, J. Íñiguez, S. Manipatruni, and R. Ramesh, Adv. Mater. **32**, 2001943 (2020).
[27] J. Li, Studies of Ultrafast processes in thin film high temperature superconductor and ferroelectric material, Ph.D. Thesis, University of Maryland at College Park, 2004.
[28] C. Wang, K.-j. Jin, Z.-t. Xu, L. Wang, C. Ge, H.-b. Lu, H.-z. Guo, M. He, and G.-z. Yang, Appl. Phys. Lett. **98**, 192901 (2011).
[29] A. J. Chiquito, C. A. Amorim, O. M. Berengue, L. S. Araujo, E. P. Bernardo, and E. R. Leite, J. Phys. Condens. Matter **24**, 225303 (2012).
[30] J. Osvald, Phys. Status Solidi (a) **212**, 2754 (2015).
[31] R. Nouchi, J. Appl. Phys. **116**, 184505 (2014).
[32] S.-C. Chang, U. E. Avci, D. E. Nikonov, S. Manipatruni, and I. A. Young, Phys. Rev. Applied **9**, 014010 (2018).
[33] A. Kolmogorov, Izv. Akad. Nauk SSSR Ser. Math **3**, 335 (1937).
[34] M. Avrami, J. Chem. Phys. **8**, 212 (1940).
[35] Y. Ishibashi and Y. Takagi, J. Phys. Soc. Jpn. **31**, 506 (1971).
[36] T. K. Song, S. Aggarwal, A. S. Prakash, B. Yang, and R. Ramesh, Appl. Phys. Lett. **71**, 2211 (1997).
[37] A. I. Khan, K. Chatterjee, B. Wang, S. Drapcho, L. You, C. Serrao, S. R. Bakaul, R. Ramesh, and S. Salahuddin, Nat. Mater. **14**, 182 (2015).
[38] Y. J. Kim, H. W. Park, S. D. Hyun, H. J. Kim, K. D. Kim, Y. H. Lee, T. Moon, Y. B. Lee, M. H. Park, and C. S. Hwang, Nano Lett. **17**, 7796 (2017).
[39] S. Smith, K. Chatterjee, and S. Salahuddin, IEEE Trans. Electron Devices **65**, 295 (2018).